# Optimisation of heaving buoy wave energy converter using a combined numerical model

Chenyu Zhao [a], Feifei Cao[a], Hongda Shi [a, b,*],

[a] College of Engineering, Ocean University of China, 238, Songling Road, Qingdao, 266100, China

[b] Shandong Provincial Key Laboratory of Ocean Engineering, 238, Songling Road, Qingdao, 266100, China

## Abstract

This optimisation study focused on the mass, dimension, hydrodynamic response, and power take-off (PTO) damping for heaving buoy wave energy converters (WEC). A numerical model, consisting of a potential flow (PF) model and a computational fluid dynamics (CFD) model, is designed and applied to address numerical errors caused by liquid viscosity after physical validations. Comparing results from the PF and CFD models, it is evident that the liquid viscosity will produce additional radiation damping for the oscillator near its resonance frequency, leading the decrease of the device's energy absorption. Optimisations based on the combined model were conducted, including non-PTO and PTO cases with both regular and irregular incident waves. The results of non-PTO cases indicate that a buoy with a relatively larger mass is more sensitive to the liquid viscosity, but it still can obtain a better optimal hydrodynamic performance with a higher wavelength-to-diameter ratio. The PTO cases compare the energy absorption caused by the linear PTO and the Coulomb PTO. The comparison results demonstrate that the Coulomb PTO can reduce the effects of viscosity and absorb more energy under identical wave conditions. This paper presents the methods and considerations for working towards the overall optimisations of the heaving buoy WEC. The work will be useful for practitioners and researcher working on wave energy utilization.



**Keywords**: wave energy converter, heaving buoy, optimisation, power take-off

## 1. Introduction

Traditional energy conversion methods based on fossil fuels represent more than 85% of the world's energy supply [1, 2]. In 2015, a deal was agreed at the United Nations Climate Change Conference in Paris to limit the global rise in temperature over the 21st century to less than two degrees above pre-industrial levels [3]. This will require reducing fossil fuel utilization and, as a result, there is an increasing need for safe, clean, and cheap renewable energy. Wave energy represents a significant component of this resource and benefits from the world-wide distribution and relatively high energy density [4, 5]. Wave energy conversion has therefore aroused considerable research and industry interests. The device, known as WEC, is designed to convert wave energy to electricity. Based on the different working principles, WEC can be broadly categorised into the oscillating water column (OWC), overtopping device (OTD), and oscillating body device (OBD) [6-8]. However, compared with traditional fossil energy, the wave energy technology is still demanding several challenges and unknowns properties, which were summarised into ten research fields by the Partnership for Research in Marine Renewable Energy (PRIMaRE) [9]. Owing to its relatively higher efficiency, OBD is considered to be a possible solution; This type of WEC absorb wave energy by the oscillator and convert it into mechanical energy and then into electricity via the PTO system [10]. According to the motion direction of the oscillator, OBD is generally classified into a point absorber, attenuator, and terminator [11]. The energy absorption capacity of a point absorber is independent of the incident wave direction because of a relatively large ratio between the incident wavelength and its oscillator's diameter.

Researchers have made efforts to enhance the extracted power from the point absorber WEC via analytical, numerical, and physical methodologies in the last several decades. Shi et al. [12] proposed a formula based on the Morison equation to seek the maximum extractions of a hydraulic system under regular waves while these results were based on the linear PTO and drag viscosity. A physical method called Wave height take-off (WHTO) based on wave height reduction was used to calculate the energy absorption of the WEC [13]. The energy capture performance of a point-absorber device under regular and irregular waves were tested in [14, 15]. The Morison drag force was used rather than the Froude–Krylov force owing to the devices' small radius. These two

references also considered the sliding friction force as a Coulomb force and applied a linear PTO. Both numerical and physical results indicated that a device without a damping plate has a slightly higher peak power and that the damping plate may offer a much higher mean power for the device. Wang et al. [16] applied a numerical means to seek the maximum output in a linear frequency-domain model. The nonlinear PTO was demonstrated to be a considerable solution to improve energy absorption. Zhang et al[17] used two symmetrically oblique springs in a point absorber design. The numerical results showed that the bi-stable PTO could dramatically develop the power capture performance compared to linear PTOs under low-frequency waves. Shi et al [18] nonlinearized the linear PTO by the ideal gas law, accurately describing the PTO force supplied by the hydraulic system with accumulators. The experiment, including a small-scale hydraulic system, validated the equation and demonstrated the gas content in the hydraulic fluid, would significantly reduce the transmission efficiency of the PTO system. In a recent study, the energy capture of the point absorber with a flexible oscillator (an airbag) was illustrated using an analytical method [19]. These explorations are then extended into the multi-DOF point absorbers. A device called the Wave Star used hemispherical oscillators to absorb energy from heave and pitch, demonstrating this design could significantly increase the whole efficiency[20, 21] and its oscillators were initially evaluated based on the potential flow[22]. In the analytical part, the hydrostatic coefficient was divided into three types to obtain a more accurate result. The physical model used a hydraulic PTO system, which could supply an approximate Coulomb damping. A tank experiment was conducted to calibrate the friction, liquid viscosity, and the PTO force, to determine the entire governing process for the device, including strong nonlinear effects. Another well-known multi-DOF device is M4, developed by the University of Manchester. The device could extract wave energy from various degrees of freedom (surge, heave, and pitch). The M4's efficiency was found to increase from 11% to 75% by optimising the hinge position and PTO damping. It was predicted that this efficiency would increase further if the device length approached half the incident wavelength[23, 24].

Numerical simulation plays a crucial role in the field of the WEC optimization. The potential flow (PF) model and computational fluid dynamics (CFD) model are always used. Each of these models has its own strengths and weaknesses. For example, the PF model can get results timely, however this model could not handle strong nonlinear

effects, especially when the wave frequency is close to the resonance frequency of a floating body. The CFD model revise these errors with a high computational cost. However, when the wave frequency is far from the natural frequency of the floating body, several nonlinear effects caused by the liquid viscosity could be ignored. As a result, this study aim to offer a speedy method to overall optimise the heaving buoy device, including its dimension, the mass of the oscillator, as well as PTO system, The remainder of this paper is organised as follows: Section 2 describes the methodology of the optimisation, including numerical and physical modelling. Section 3 introduces optimisation results for PTO and non-PTO cases. Conclusions are drawn in Section 4.

## 2. Optimisation methods

### 2.1 Experimental methods

#### 2.1.1 Layout

The physical experiment was conducted in a 60m long, 3m wide, and 1.5m deep flume equipped with a single-directional wave maker. A porous medium was used as the wave absorber. The distance from the wave maker to the physical model was 25 m to ensure the stability of the incident wave. During tests, the water depth was set to be 0.8 m. The details of the experimental layout are shown in Figure 1.

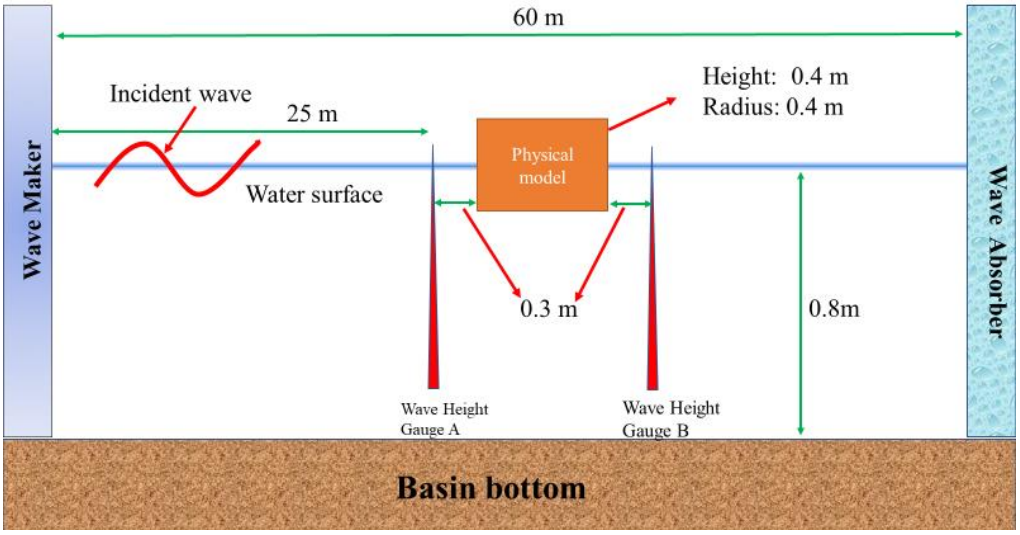


Figure 1: Layout of physical test: two wave gauges are used to collect wave data ahead of and behind the physical model

#### 2.2.2 Physical model

The model employed in the test was a typical point absorber with a cylinder heaving

buoy as its extractor. The mass of the buoy was 102 kg, and its dimension is listed in Table 1. Along the outer circle of the buoy, there were three linear bearings to ensure that the buoy heaved along three light bars with very little resistance. The displacement of the buoy was recorded by a displacement sensor and ranged from 0 m to 0.5 m with an accuracy of 0.1%. The details are shown in Figure 2.

Table 1 The dimension of the buoy

| Property | |
|---|---|
| Diameter | 0.8 m |
| Height | 0.4 m |


Figure 2: Physical model: Buoy is restricted to heave along three light bars via linear bearings with little friction

### 2.2.3 Cases

The physical experiment included a decay test and free oscillation test (non-PTO and PTO cases). In the decay test, the buoy was released from a unbalanced position and a displacement sensor would record the motion of the buoy [see Figure 3 (a)]. For the non-PTO oscillation test, the buoy operates without any PTO damping. The incident waves in north China are sheltered and blocked by the island chain in the western Pacific. Considering typical wave conditions in Qingdao[25], the experimental scale

ratio, and the capability of the wavemaker system, the wave parameters used in this experiment are listed in Table 2. All incident waves were regular. During the PTO cases, a rack was installed at the central point of the upper surface of the buoy. As the buoy heaved, the rack drives the magnetic powder brake, which can offer different Coulomb damping on its connected shaft by various input electric currents [presented in Figure 3 (b)].

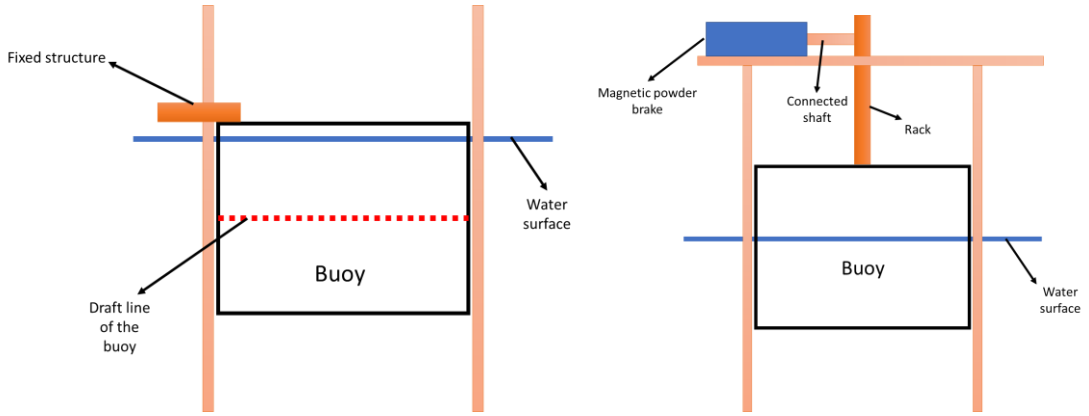


(a) (b)

Figure 3: (a) Decay test, step 1. the buoy is limited below its balanced position by the fixed structure; step 2. The buoy is released, and its decay curve could be obtained; (b) PTO oscillation test, the PTO damping is provided by a magnetic powder brake

Table 2 Parameters of the incident wave used during physical test

| Case number | Wave Height H | Wave period T |
|---|---|---|
| 1 | 0.12 m | 2 s |
| 2 | 0.084 m | 1.16 s |

## 2.2 Numerical methods

### 2.2.1 Model illustration

In this combined concept, the CFD model only calculates the added mass and radiation damping via decay and forced oscillating cases without any incident wave generating. As a result, a smaller numerical wave tank that meets the requirements of radiation wave absorption can be applied, dramatically reducing the computational cost. Based on results from these decay and forced motion cases, the PF time-domain model recalculates oscillator motion. Figure 4illustrates the flow chart of the combined

concept.

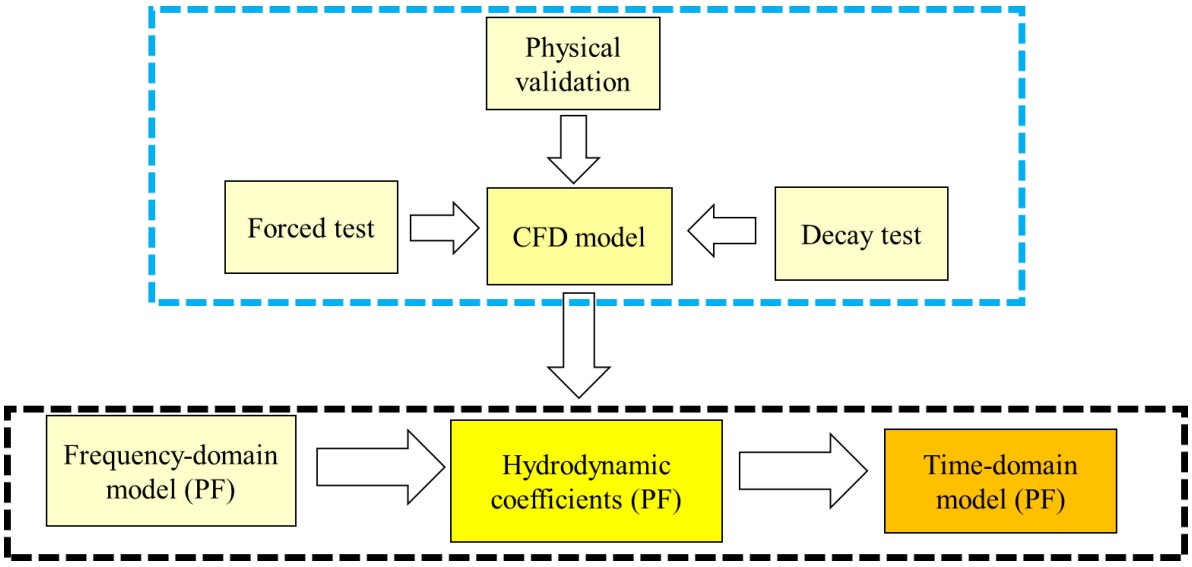


Figure 4: The flow chart of the combined numerical model.

The governing equation for the heaving buoy

$$m\ddot{x} = F_r + F_e + F_{PTO} + F_M + cx \tag{1}$$

where $m$ is the mass of the buoy, $F_r$ is the radiation force, $F_e$ is the exciting force, $F_{PTO}$ is the PTO force, and $F_M$ is the mooring force. The variable $c$ is the hydrostatic stiffness coefficient owing to the buoyancy and is constant here for sufficiently small deflections of the body.

The $j-$th radiation force owing to the diffraction wave induced by the $k-$th unit amplitude body rigid motion is

$$F_{rjk} = -i\omega\rho \int_{S_{wet}} \varphi_{rk}\left(\vec{X}\right) n_j dS \tag{2}$$

The radiation potential $\varphi_{rk}$ can be presented as real and imaginary parts that produce added mass and radiation damping.

$$F_{rjk} = \omega^2 a(\omega) + i\omega b(\omega) \tag{3}$$

where the added mass and damping are

$$a(\omega) = \frac{\rho}{\omega} \int_{S_{wet}} Im\left[\varphi_{rk}\left(\vec{X}\right)\right] n_j dS \tag{4}$$

$$b(\omega) = -\rho \int_{S_0} Re\left[\varphi_{rk}\left(\vec{X}\right)\right] n_j dS \tag{5}$$

When the buoy heaves near its resonance frequency, $a(\omega)$ and $b(\omega)$ are significantly influenced by the liquid viscosity; hence, the viscosity effects will be revised in the CFD model by decay and forced tests.

For non-PTO situations, a decay curve (as shown in Figure 5) and a fitted curve by the peak point can be obtained to determine the revised $a(\omega)$ and $b(\omega)$ on the resonance period $T_n$ .

$$a(\omega_n)_{revised} = \frac{c}{\omega_n^2} - m \tag{6}$$

$$b(\omega_n)_{revised} = \frac{2kc}{\omega_n^2} \tag{7}$$

For the heaving buoy, $c = \rho g S_{area}$, where $\rho$ is the water density, and $S_{area}$ is the area of the bottom face.

$k$ can be obtained by a fitted curve. This method can be seen [26].

$$k = \frac{1}{2\pi} ln\left\{\frac{F(t)}{F(t+T_n)}\right\} \tag{8}$$

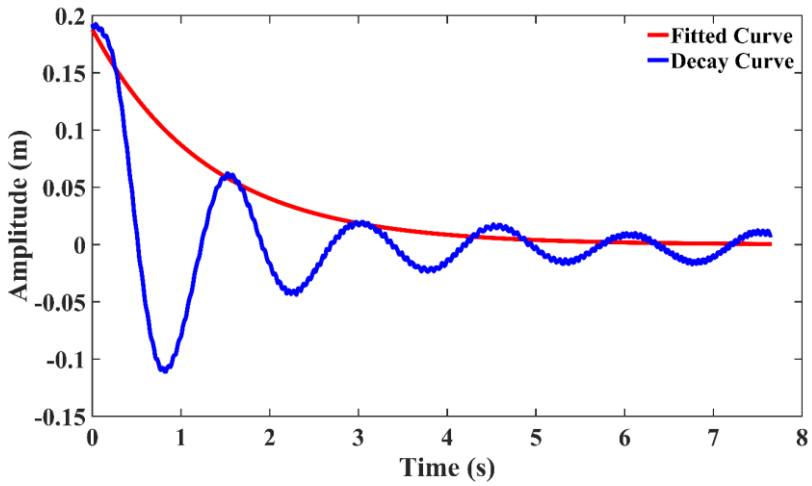


Figure 5: Example of the decay curve and fitted curve via peak point

During the forced cases, $a(\omega)$ and $b(\omega)$ can be calculated as

$$a(\omega)_{revised} = \frac{c - \frac{F_a}{z_a}\cos\theta}{\omega^2} - m \tag{9}$$

$$b(\omega)_{revised} = \frac{\frac{F_a}{z_a}\sin\theta}{\omega} \tag{10}$$

where $F_a$ is the amplitude of the external force, and $\theta$ is the phase difference between the external force and the motion of the buoy. The liquid viscosity does not significantly influence the exciting forces (diffraction and FK force) during the resonance cases[27]. During PTO situations, linear damping and coulomb damping are applied.

The linear PTO force $F_{PTO}$ is proportional to buoy velocity.

$$F_{PTO} = -C_{PTO}\dot{z}(t) \tag{11}$$

where $-C_{PTO}\dot{z}(t)$ is a damping caused by energy extraction.

The Coulomb PTO force is calculated as:

$$F_{PTO} = -sign\left(C_{PTO}, \dot{z}(t)\right) \tag{12}$$

where the direction of the damping force is always opposite to the velocity when the amplitude is a constant value.

A linear PTO does not the alter motion frequency of the buoy, the $b(\omega)_{revised}$ will be converted into $b(\omega)_{revised} = \frac{\frac{F_a}{z_a}\sin\theta}{\omega} - C_{PTO}$.

For the Coulomb PTO, the external force is considered large enough to maintain the buoy motion as a sine one. For the buoy heave motion, the (1) is transformed into

$$\left(m + a(\omega)\right)\ddot{z}(t) + b(\omega)\dot{z}(t) + cz(t) + F_{PTO} = F_a sin(\omega t + \theta) \tag{13}$$

$$\ddot{z}(t) = \omega^2 z_a \sin(\omega t)\ ,\ \dot{z}(t) = \omega z_a \cos(\omega t), \mathrm{z(t)} = z_a \sin(\omega t) \tag{14}$$

Add (14) into (13), and when $\mathrm{t} = 0$

$$b(\omega)_{revised} = \frac{F_a \sin(\theta) - F_{PTO}}{\omega z_a} \tag{15}$$

when $t = \frac{\pi}{2\omega}$,

$$a(\omega)_{revised} = \frac{c - \frac{F_a}{z_a}\cos\theta - \frac{F_{PTO}}{z_a}}{\omega^2} - m \tag{16}$$

### 2.2.2 Model validation

The CFD model (FLOW-3D [28]) and PF model (AQWA [29]) are validated in this section. The CFD model houses two NWTs. The smaller one (NWT A) which does not include any incident waves is used in the combined model and the relatively larger one (NWT B) which can generate waves is applied to compare the results differences from these three models (Figure 6). NWTs boundary conditions are illustrated in Table 3. For both CFD NWTs, the mesh size is refined around the waterline (Figure 7). Figure 8 shows the result of the mesh resolution study, indicating the mesh with $r_m = 10$ (the ratio between buoy height and cubic mesh length) in the refined zone can meet the accurate requirements. As shown in Figure 9, the results from the two NWTs are almost identical, and an excellent agreement between the CFD results and the experimental results is observed. The slight differences between numerical and physical results are supposed to be caused by the minute Coulomb friction between the linear bearing and the light bar.

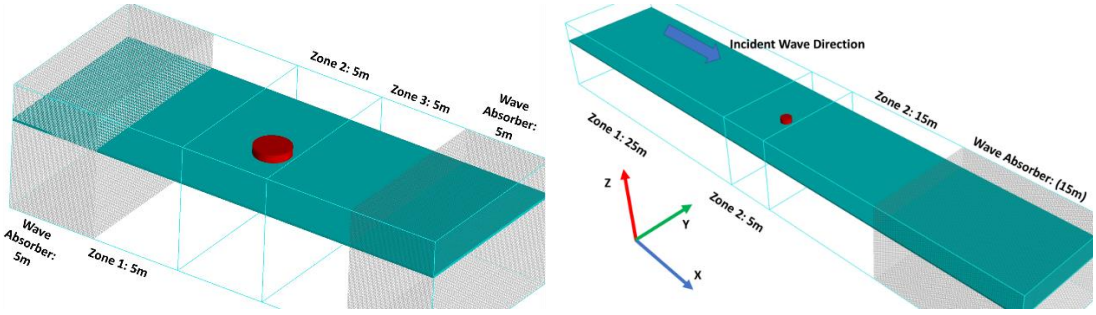


(a) (b)

Figure 6: Two CFD NWTs: (a) NWT A without incident wave, used in the combined model; (2) NWT B with incident wave, used in the CFD model.

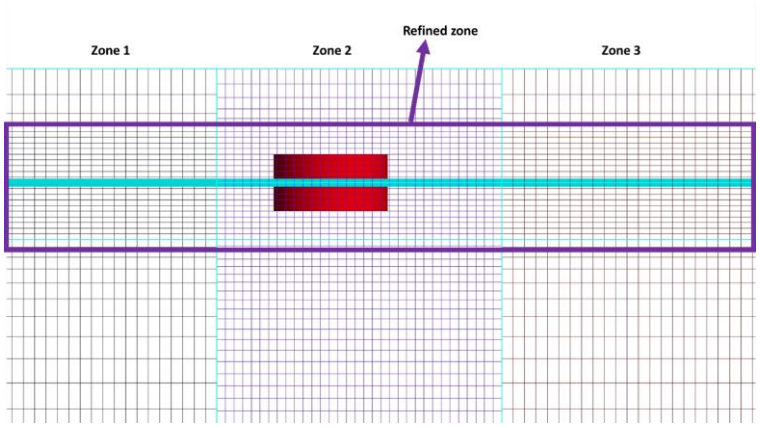


Figure 7: The mesh in zone 2 is finer than that in zone 1 and zone 3, the changing ratio of mesh size is 1.25; Refinement of the mesh size around the waterline is used in all zones. The mesh size in the refined zone 2 is $r_m = 10$

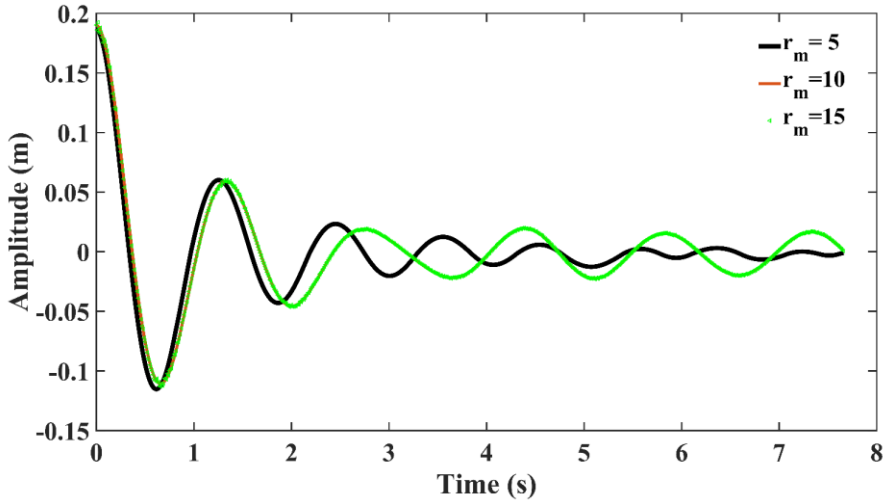


Figure 8: The mesh resolution study of the CFD model: No significant differences are observed between $r_m = 10$ and $r_m = 15$

Table 3 Boundary conditions of NWT

| | Zone 1 | Zone 2 | Zone 3 |
|---|---|---|---|
| $X_{min}$ | Outflow with wave absorber (NWT A), Waves (NWT B) | Symmetry | Symmetry |
| $X_{max}$ | Symmetry | Symmetry | Outflow with wave absorber |
| $Y_{min}$ | Symmetry | Symmetry | Symmetry |
| $Y_{min}$ | Symmetry | Symmetry | Symmetry |
| $Z_{min}$ | Wall | Wall | Wall |
| $Z_{max}$ | Specified pressure | Specified pressure | Specified pressure |

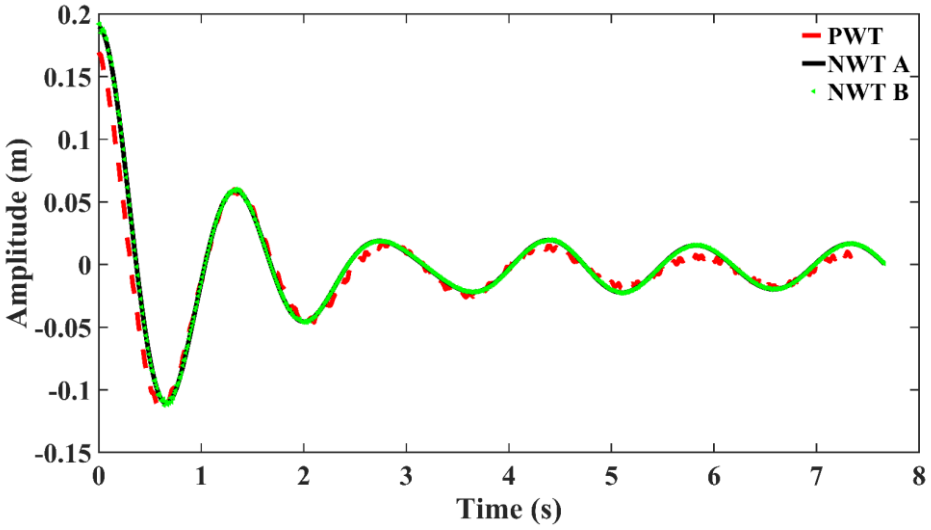


Figure 9: Results obtained by CFD model and physical test

For the free-oscillation cases, the results from the experiment, PF, and CFD are illustrated in the Figure 10. The PF and CFD models could be validated by the physical results used in the model test. As shown in Figure 10, the amplitude of the buoy heave motion in the PF model was slightly larger than that in the PWT and CFD. This is believed to be the result of energy losses that is ignored in PF models.

The validation of PTO cases is presented in the Figure 11. The motion frequency of the buoy in two numerical have a good agreement with the results of the physical experiment, while the amplitude differences are observed. The differences in PF model are caused by mechanical energy loss from the PTO and the effect of viscosity. The difference in the CFD model is smaller than that in the PF model, owing to the CFD model has calculated these viscous energy losses.

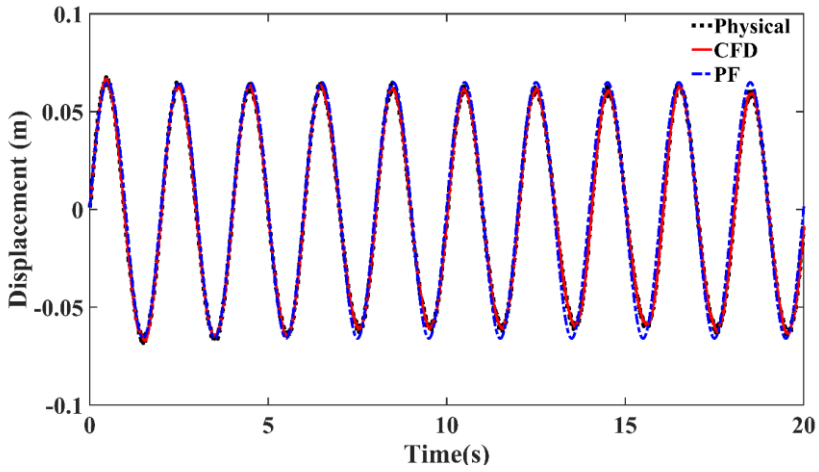


(a)

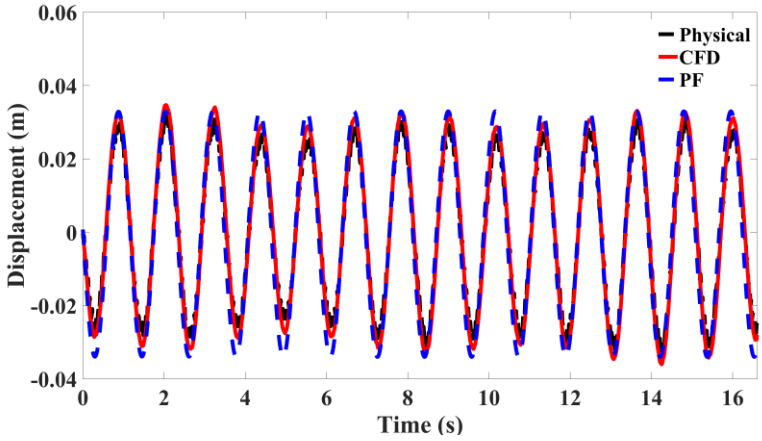


(b)

Figure 10: Validation of numerical model, comparing physical model measurements and numerical model predictions of heaving buoy displacement with regular waves: (a) $T = 2\ s$ and $H = 0.12\ m$, and (b) $T = 1.16\ s$ and $H = 0.084\ m$

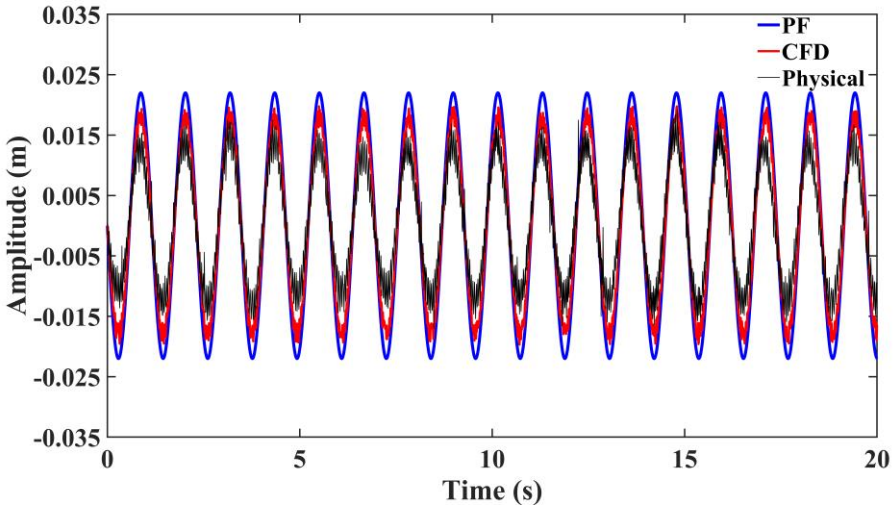


Figure 11: Validation of PTO cases: the incident wave is $T = 1.16\ s$ and $H = 0.084\ m$ and the Coulomb damping is 20 N

## 3. Optimisation results

The heaving buoy hydrodynamic response and PTO damping simultaneously determine the energy absorption of the device. In this section, the optimisation results are presented in non-PTO cases and PTO cases. During this part, two normalised parameters are defined to evaluate the dimension and mass of the heaving buoy. The first one is $r_1$, defined as the wavelength of incident wave $\lambda$ and normalised by the diameter of the heaving buoy $D$, which shows the dimension effects. The other one presenting the mass effects is $r_2$, the ratio between the draft and the height of the buoy. All optimisations are conducted under both regular and irregular waves.

### 3.1 Optimization without PTO

#### 3.1.1 The effects of viscosity on hydrodynamic response

The motion amplitude of the buoy will obviously increase during the wave amplitude grows. Therefore, the RAO, defined as the ratio between the amplitude of the buoy motion and the wave amplitude, is used to describe the buoy motion amplitude. To validate the accuracy of the combined model, the CFD model is also used in these cases. Figure 12 shows the RAO of three buoys with different $r_2$ under the PF, CFD, and combined models. It is found that the resonance phenomena are not apparent in the PF

model for cases with smaller $r_2$. This is caused by the large hydrostatic coefficients of the light buoy [shown in Figure 12 (a)]. The stable RAO changing trend in Figure 12 (a) demonstrates the motion of the buoy with a smaller $r_2$ is not very sensitive to $r_1$. However, the significant RAO peak can be seen in cases with the relatively heavier buoys [Figure 12(b) and Figure 12(c)].

Comparing the results calculated by the three models, it is found that the peak RAO amplitude of PF model is more significant than that in the other two models, and the largest difference appears in the case of resonance. A slightly larger amplitude (compared with CFD results) is still found in the combined model, which is caused by vortex along the sharp edge of the buoy (see Figure 13). The combined model cannot consider these effects of the vortex, which accounts for the high-order velocity items.

Table 4 lists $a(\omega)$ and $b(\omega)$ of the buoy with $r_2$ = 0.5 in the PF and CFD models under three incident waves. The differences in $a(\omega)$ are insignificant in all cases, even in the resonance case (only 1.4%), while the $b(\omega)$ resonance difference is quite vast (315%). The results can demonstrate that the viscosity mainly affects the radiation damping rather than the added mass.

Table 4 $a(\omega)$ and $b(\omega)$ for buoy with $r_2$ = 0.5; $r_1$= 4.64 is resonance case.

| $r_1$ | PFa(ω) | CFDa(ω) | PF b(ω) | CFD b(ω) | Difference a(ω) | Difference b(ω) |
|---|---|---|---|---|---|---|
| 3.50 | 206 | 207 | 106 | 114 | 0.48% | 7.5% |
| 4.64 | 210 | 213 | 160 | 500 | 1.4% | 315% |
| 6.02 | 213 | 214 | 173 | 177 | 0.47% | 2.31% |

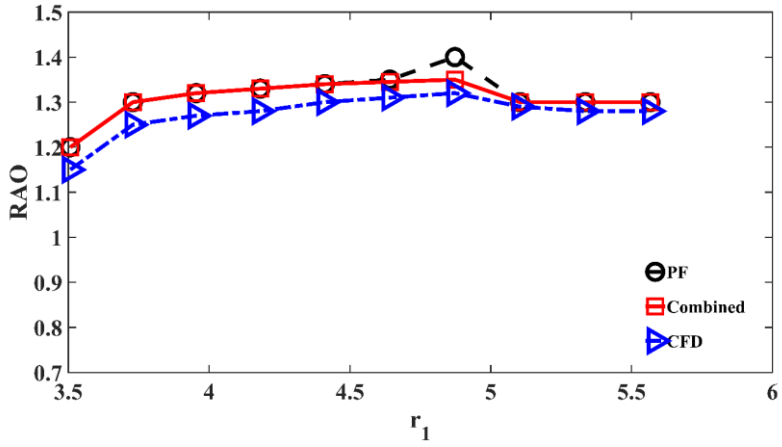


(a)

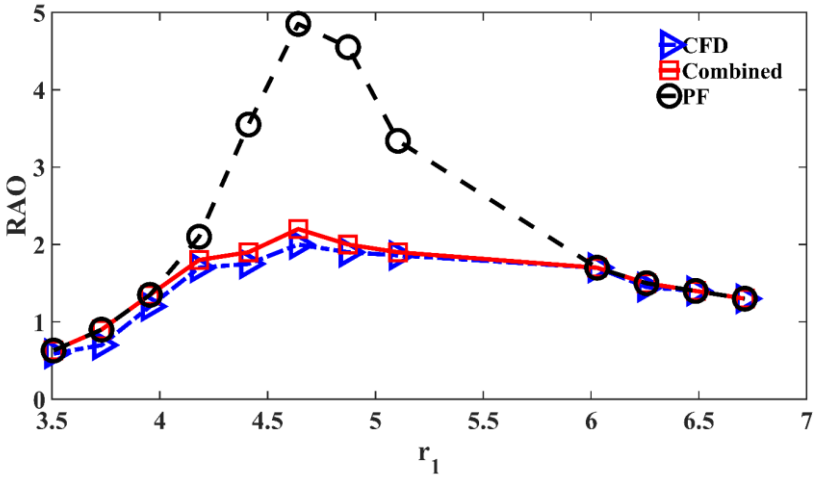


(b)

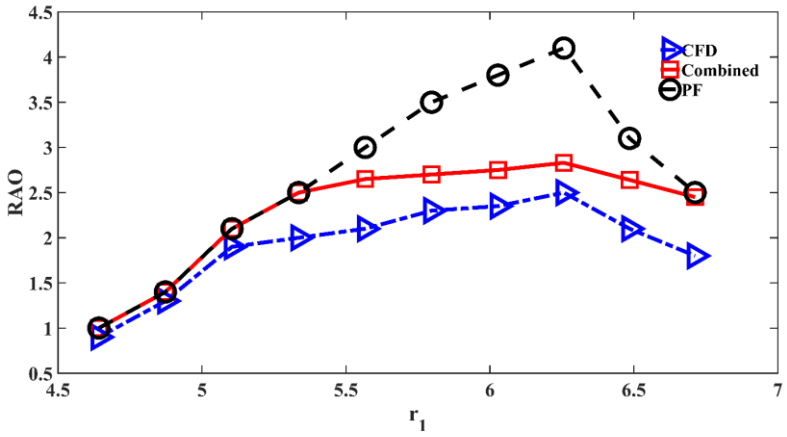


(c)

Figure 12: RAO of buoys with different $r_2$ calculated by CFD, PF, and combined numerical models: (a) $r_2$= 0.2, (b) $r_2$= 0.5, and (c) $r_2$= 0.7

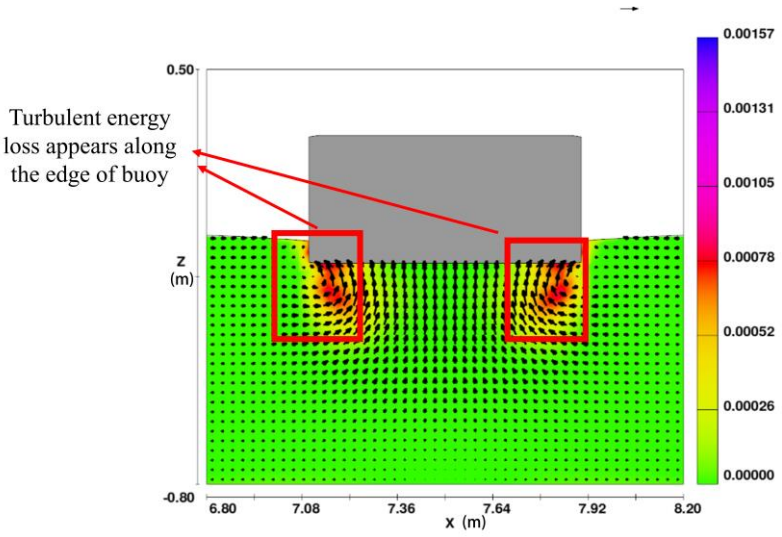


Figure 13: Turbulent energy loss during buoy motion in the CFD model: almost all turbulent energy loss appears along the edge of buoy

### 3.1.2 Regular wave cases

Figure 14 presents different buoy RAOs under the combined model. The optimal $r_1$ of the heaving buoy increases with a growing $r_2$. The peak RAO of the $r_2 = 0.2$ buoy is not obvious, which means a heavier buoy is an advantage in the device design. Also, a buoy with a larger $r_2$ has a wider $r_1$ range to obtain the relatively high RAO (for $r_2$= 0.7, the RAO is always higher than 2 from $r_1$= 6 to $r_1$= 7). Considering the large incident wavelength (compared to the radius of the oscillators) under the real sea environment, a buoy with a higher $r_2$ is believed to have a better hydrodynamic response in most situations.

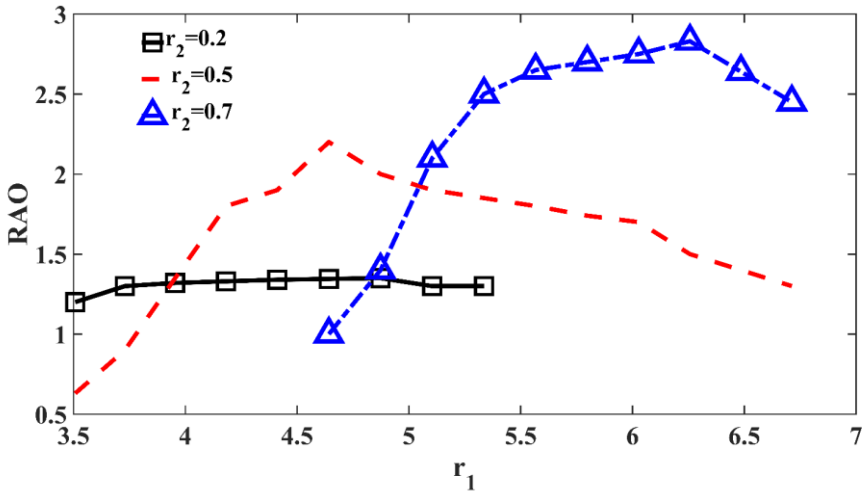


Figure 14: RAO of different buoys under various $r_1$

### 3.1.3 Irregular wave cases

The performance of the heaving buoy under irregular waves is more critical for the device design because the wave conditions in irregular cases are more similar to the real sea environment. The irregular wave is defined by a JONSWAP spectrum with a 1-m significant wave height ($H_s$) and 4-s peak wave period ($T_p$). The gamma value for the JS spectrum is 3.3. The displacement of the buoy and the water surface elevation were converted into the frequency domain by a Fourier transform (shown in Figure 15). The buoy with a greater $r_2$ also has a better hydrodynamic response under irregular waves. The buoy with $r_2$= 0.7 exhibits a better response under low-frequency wave conditions compared with the other two cases because of the large inertia.

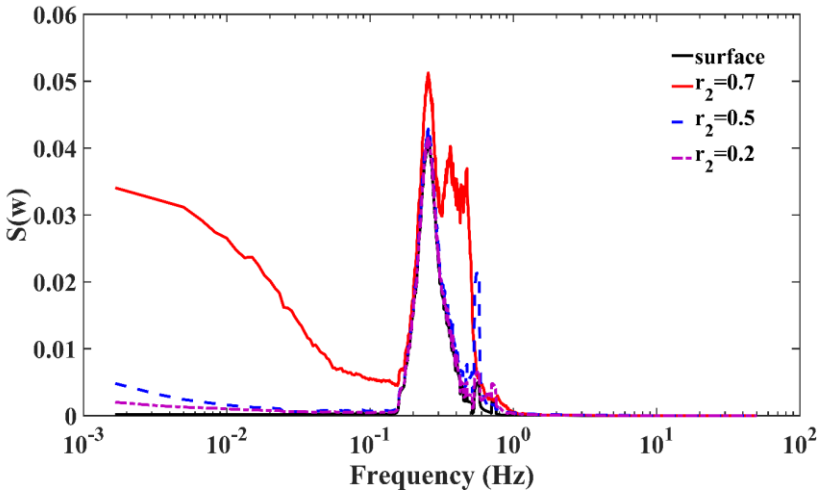


Figure 15: Displacement spectrum of $r_2$= 0.7 buoys compared with wave spectrum

### 3.1.4 Summary

This section presented the optimisation results of non-PTO cases. The buoy with a larger $r_2$ is more sensitive to the viscous effects, and the buoy needs to match a larger $r_1$to get its peak RAO. Generally, a heavier buoy is demonstrated to have a higher peak RAO in regular wave cases and a more rigid motion in irregular wave cases.

## 3.2 Optimization with PTO

The buoy capture width $C_{capture}$, is applied to evaluate its capture performance.

$$C_{capture} = \frac{P_{absorb}}{P_{wave}} \tag{17}$$

where $P_{absorb}$ is the absorbed power of WEC, and $P_{wave}$ is the wave power of the unit wave crest length.

The power of the regular wave,

$$P_{wave} = \frac{\rho g A^2}{4\omega} \tag{18}$$

where $\rho$ is the water density, $g$ is the acceleration of gravity, and $A$ is the amplitude of the incident wave.

The power of the irregular wave,

$$P_{wave} = \frac{\rho g^2 H_s^2}{64\pi} T_e \tag{19}$$

where $T_e$ is the wave energy period for the JS spectrum (gamma value 3.3), and $T_e = 0.9T_p$. [30]

### 3.2.1 The effects of viscosity on capture performance

Figure 16(a) presents the capture width of the buoy ($r_2$ = 0.5) with linear PTO damping under its optimal incident wave frequency ($r_1$ = 4.64). It is observed that the liquid viscosity strongly reduces the buoy energy absorption during cases with small damping. That means the energy loss caused by the liquid viscosity should not be ignored in these cases. However, when the damping is stiff enough, the differences of $C_{capture}$ in two models are unapparent. The insignificant viscous energy loss in these stiff damping cases is led by small buoy velocity. When the PTO coefficients are equal to the buoy radiation coefficients, the buoy will obtain maximum absorption[31]. Owing to the influence of liquid viscosity on the radiation damping (see Table 4), the optimal PTO coefficients in two models have a resulting difference (500 N/m/s in the combined model and 160 N/m/s in the PF model).

For the buoy with Coulomb PTO [shown in Figure 16 (b)], the changing trends of the capture width are identical in the PF and combined models, indicating the viscosity does not alter the optimal Coulomb PTO damping. The energy absorption differences between two models in Figure 16 (b) are smaller than that in Figure 16 (a). To explore the reason for this, Figure 17 presents the buoy heave displacement with the optimal linear and Coulomb PTO (500 N/m/s for linear damping and 120 N for Coulomb damping) in the CFD model, respectively. The results present an identical motion frequency of the buoy under the two PTO types, while a smaller motion amplitude in coulomb PTO case is observed, which means a smaller energy loss caused by the

viscosity in the coulomb PTO cases.

By comparing the energy absorption in the combined model, Coulomb PTO always has a better performance. Moreover, the Coulomb force can be easily controlled via a hydraulic system with accumulators to smooth the fluctuant power output in the real sea environment[32].

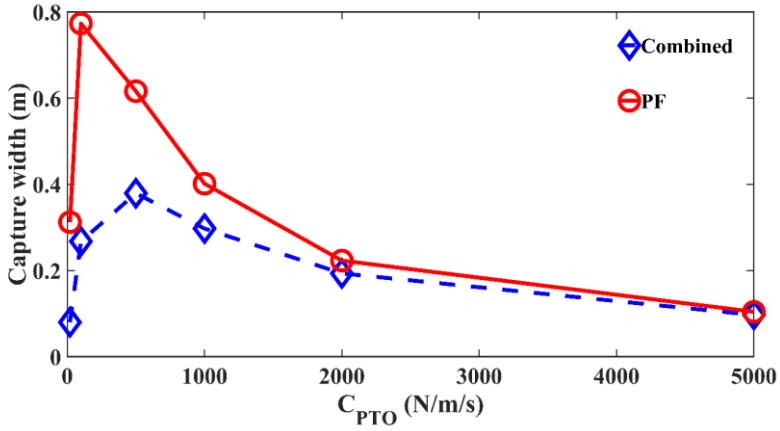


(a)

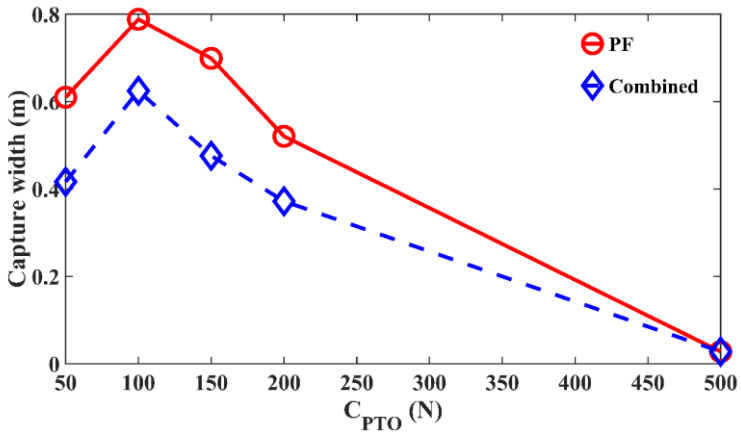


(b)

Figure 16: Capture width of the buoy ($r_2 = 0.5$) equipped in PF and combined models: (a) linear damping; optimal $C_{capture}$ is 0.36 m and 0.8 m in the combined model and the PF model, respectively. (b) Coulomb damping; optimal $C_{capture}$ is 0.6 m and 0.8 m in the combined model and PF model, respectively

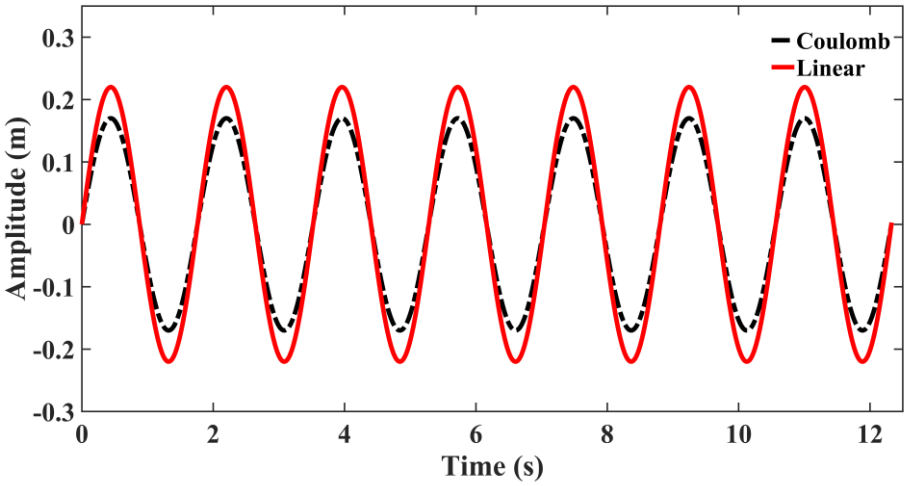


Figure 17: Heave displacement amplitude of buoy with two PTO types ($r_2 =$ 0.5 and $r_1 = 4.64$): 0.17 m for Coulomb damping and 0.22 m for linear damping

### 3.2.2 Regular wave cases

The capture performance of the buoy calculated by the combined model is presented in a cloud chart (Figure 18). The relatively higher energy absorption cases in Figure 18 (a) distribute from $r_1$= 4 to $r_1$= 5, while similar cases in Figure 18 (b) have a broader distribution, from $r_1$= 4 to $r_1$= 6. The distribution difference determines that the Coulomb damping is less sensitive to $r_1$ than linear damping. Also, a significantly higher peak $C_{capture}$ is observed in Coulomb damping cases (0.36 m for linear damping and 0.6 m for Coulomb damping). The optimal $r_1$ are almost the same for the two damping types, demonstrating the optimal $r_1$ is not sensitive to the damping type.

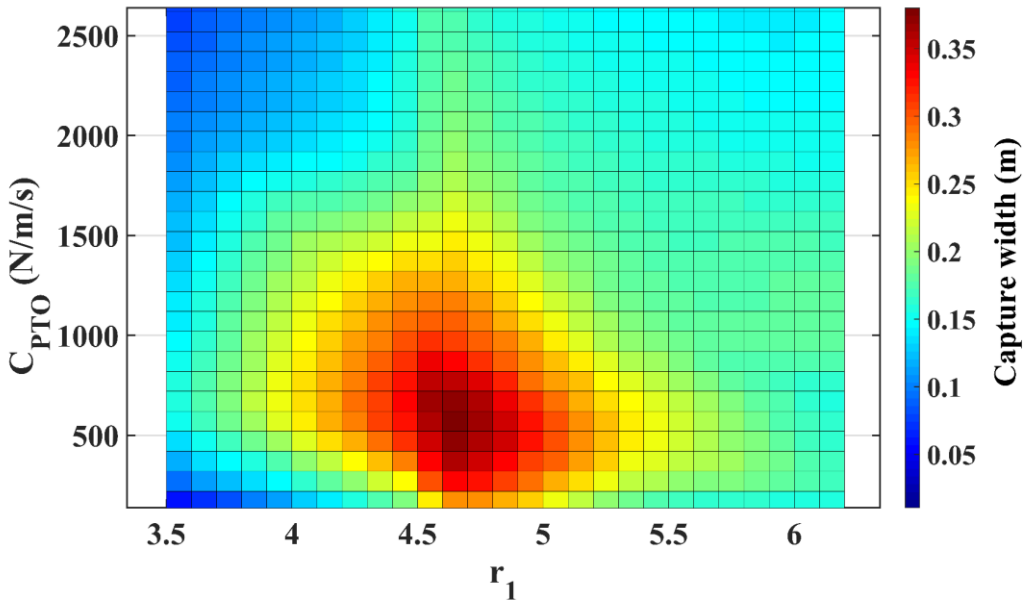


(a)

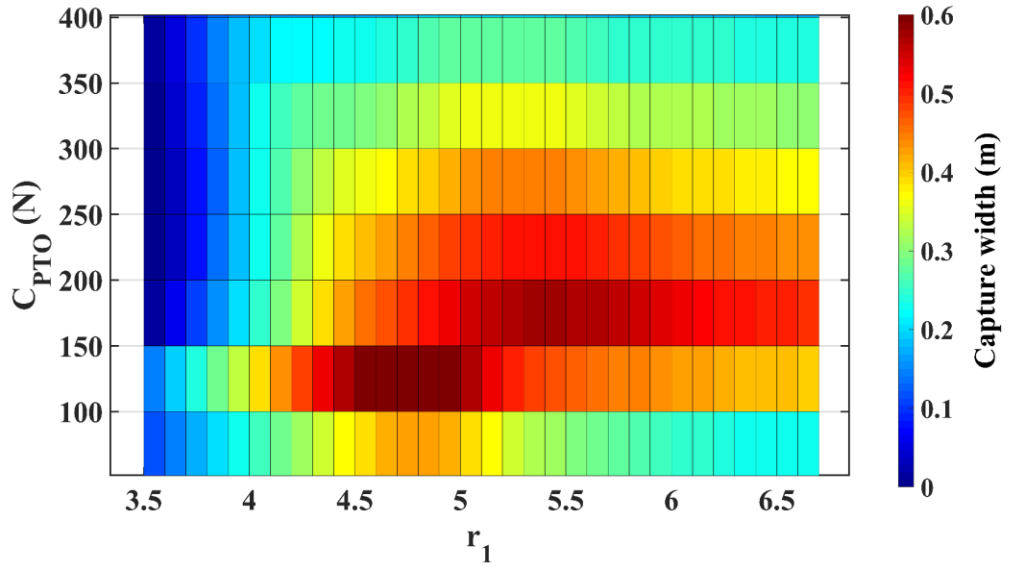


(b)

Figure 18: $C_{capture}$ of buoys ($r_2$= 0.5) with (a) linear and (b) Coulomb damping. Optimal $C_{PTO}$ for the two damping types are 500 N/m/s and 120 N and the optimal $C_{capture}$ are 0.36 m and 0.6 m

The capture performance of a heavier buoy ($r_2$= 0.7) is then illustrated (see Figure 19). Compared with Figure 18 (a), the $r_2$= 0.7 buoy is better adapted not only to the incident wave (from $r_1$= 4.5 to $r_1$= 7) but also to $C_{PTO}$. Its peak $C_{capture}$ can reach 0.8 m, which is more than twice that in the $r_2$= 0.5 buoy. The optimal $C_{PTO}$ is also near 500 N/m/s

but the optimal $r_1$ becomes larger (4.6 for the $r_2$= 0.5 buoy and 5.7 for the $r_2$= 0.7 buoy). For both damping types, a heavier buoy can always have a better capture performance, and this mass effect seems to be more significant for the linear damping (0.36 m to 0.8 m under linear cases, and 0.6 m to 1 m for Coulomb damping). Comparing to the linear damping, the Coulomb damping still has better energy absorption in the $r_2$= 0.7 buoy cases.

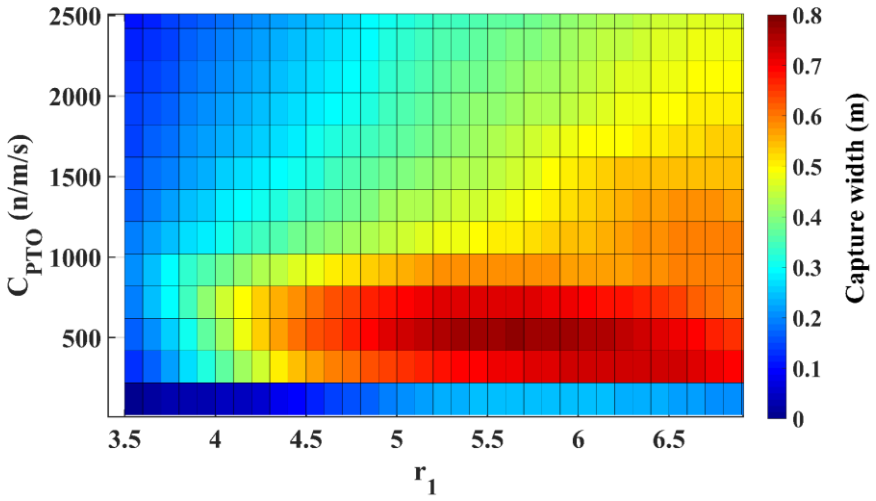


(a)

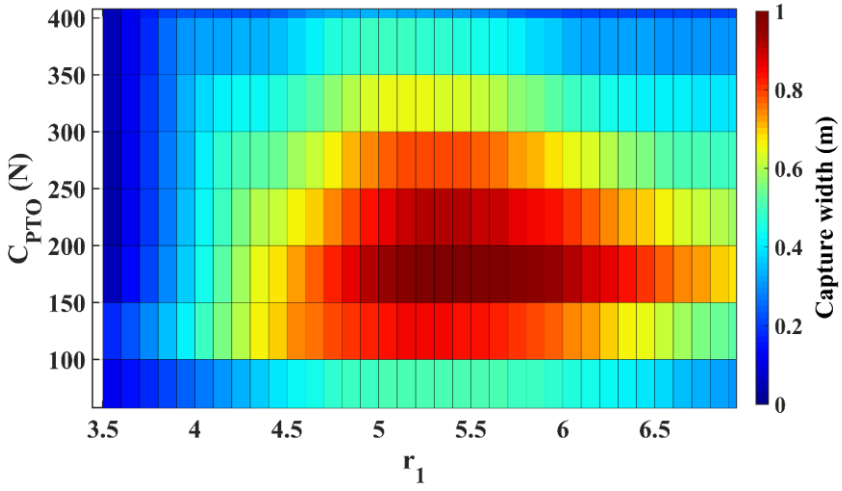


(b)

Figure 19: $C_{capture}$ of buoys ($r_2$= 0.7) with (a) linear and (b) Coulomb damping. Optimal $C_{PTO}$ for the two damping types are 580 N/m/s and 175 N; Optimal $C_{capture}$ are 0.36 m and 0.6 m Optimal $C_{capture}$ is 0.8 m for linear damping and 1 m for Coulomb damping

### 3.2.3 Irregular wave cases

The input wave condition is identical to that in section 3.1.3. The displacement of $r_2$= 0.7 buoy with different PTO under irregular waves is shown in Figure 20. The primary frequency of the buoy motion has an excellent agreement with the wave frequency in all cases, but the large damping will reduce its motion amplitude. The results illustrate that the buoy motion frequency is still not very sensitive to the damping type and amplitude in irregular cases. In the comparison of damping type, the Coulomb damping still exhibits a better capture performance under irregular waves (see Figure 21, 1.27 m for linear damping and 1.58 m for Coulomb damping). For this irregular wave, the effect of viscosity can be ignored because of the relatively large optimal PTO amplitude (5000 N/m/s for linear damping and 1000 N for Coulomb damping).

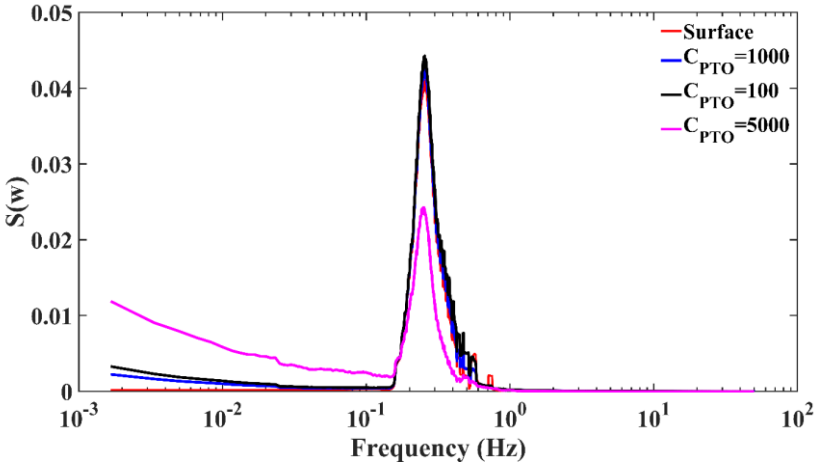


(a)

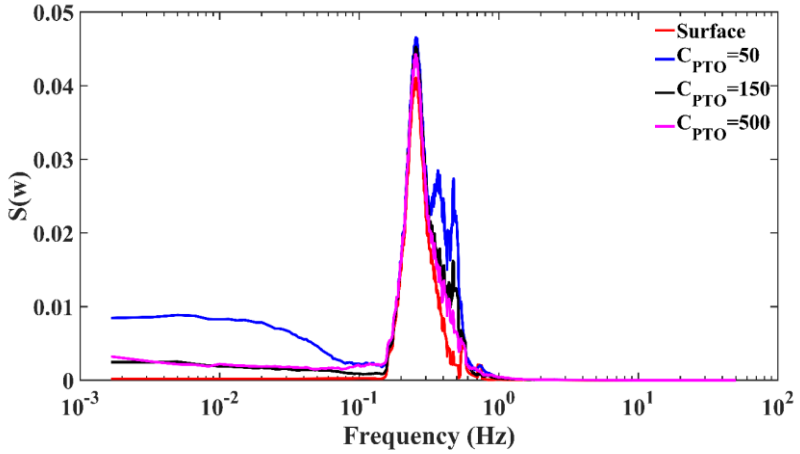


(b)

Figure 20 Hydrodynamic response of $r_2$= 0.7 buoy under (a) linear and (b) Coulomb damping under irregular waves

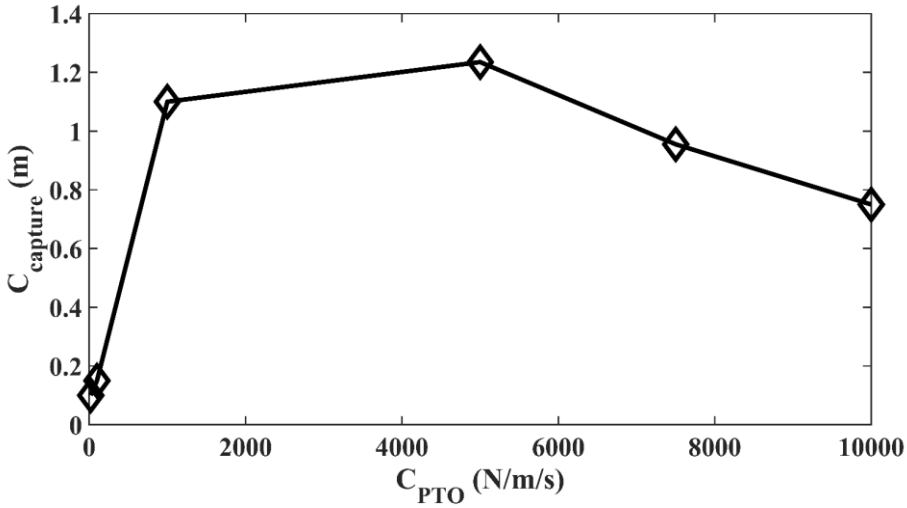


(a)

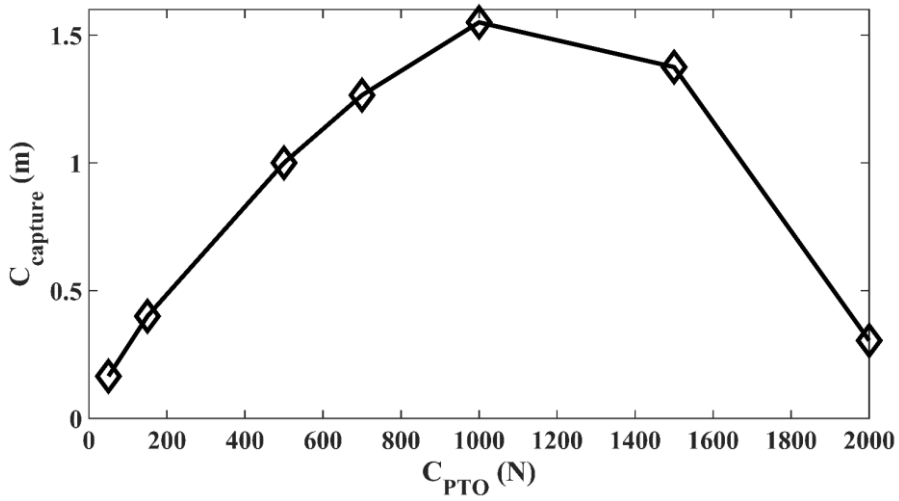


(b)

Figure 21: $C_{capture}$ of $r_2$= 0.7 buoy with (a) linear damping and (b) Coulomb damping

### 3.2.4 Summary

This section presented the comparison results of the energy capture performance of the heaving buoy with different PTO and oscillators. Compared with the linear damping, the Coulomb damping can reduce the effect of viscosity and absorb more energy. For the oscillators, a heavier buoy always performed better in energy absorption under both regular and irregular incident waves.

# 4. Conclusions

This study used a combined numerical model to optimise a heaving buoy device, including oscillators and PTO. After comparing results from the validated PF and CFD model, it is believed that the combined model could effectively revise the numerical errors caused by the effects of viscosity. The liquid viscosity would produce a significant additional radiation damping when the wave frequency is close to the buoy resonance frequency, reducing the buoy motion and energy absorption. With the combined model, the optimisations include non-PTO and PTO situations.

In the non-PTO optimisations, a heavier buoy is more sensitive to the liquid viscosity, while it still had a better hydrodynamic response than a lighter buoy in the combined model. The heavier buoy needs to match a greater wavelength-to-diameter to get its optimal RAO.

In the PTO optimisations, linear and Coulomb PTO damping types were discussed. It was found that the effects of viscosity were less significant in Coulomb damping cases. The buoy with a larger mass exhibited a better capture performance, and this effect is independent on the PTO types. Additionally, the buoy with Coulomb damping always had a better capture performance under regular and irregular waves.

Future optimisations will focus on multi-freedom point absorbers.

## Acknowledgements

The author would like to acknowledge the support of the Innovative Technology Research and Development of Efficient Utilization of Marine Energy based on China's Resource Characteristics (Grant No. 2018YFB151900), the Qingdao Municipal Science & Technology Program (15-8-3-7-jch) and Special Project for Marine Renewable Energy (GHME2016YY02).

# References


[1] Murphy DJ, Hall CA. Energy return on investment, peak oil, and the end of economic growth. Annals of the New York Academy of Sciences. 2011;1219:52.
[2] Bardi U. Peak oil: The four stages of a new idea. Energy. 2009;34:323-6.
[3] Robbins A. How to understand the results of the climate change summit: Conference of Parties21 (COP21) Paris 2015. Springer; 2016.
[4] Appendini CM, Urbano-Latorre CP, Figueroa B, Dagua-Paz CJ, Torres-Freyermuth A, Salles PJAe. Wave energy potential assessment in the Caribbean Low Level Jet using wave hindcast information. 2015;137:375-84.
[5] Morim J, Cartwright N, Etemad-Shahidi A, Strauss D, Hemer MJAe. Wave energy resource assessment along the Southeast coast of Australia on the basis of a 31-year hindcast. 2016;184:276-97.
[6] Sheng W. Wave energy conversion and hydrodynamics modelling technologies: A review. Renewable and Sustainable Energy Reviews. 2019;109:482-98.
[7] He F, Huang Z. Hydrodynamic performance of pile-supported OWC-type structures as breakwaters: an experimental study. Ocean Engineering. 2014;88:618-26.
[8] He F, Huang Z, Law AW-K. An experimental study of a floating breakwater with asymmetric pneumatic chambers for wave energy extraction. Applied energy. 2013;106:222-31.
[9] Greaves D, Iglesias G. Wave and tidal energy: John Wiley & Sons; 2018.
[10] SAFABAKHSH M, Dubey C, Bordmann JJ. Power take off system for wave energy converter buoy. Google Patents; 2019.
[11] Drew B, Plummer AR, Sahinkaya MN. A review of wave energy converter technology. Sage Publications Sage UK: London, England; 2009.
[12] Shi H, Cao F, Liu Z, Qu N. Theoretical study on the power take-off estimation of heaving buoy wave energy converter. Renewable energy. 2016;86:441-8.
[13] Shi H, Zhao C, Hann M, Greaves D, Han Z, Cao F. WHTO: A methodology of calculating the energy extraction of wave energy convertors based on wave height reduction. Energy. 2019.
[14] Beatty SJ, Bocking B, Bubbar K, Buckham BJ, Wild P. Experimental and numerical comparisons of self-reacting point absorber wave energy converters in irregular waves. Ocean Engineering. 2019;173:716-31.
[15] Beatty SJ, Hall M, Buckham BJ, Wild P, Bocking B. Experimental and numerical comparisons of self-reacting point absorber wave energy converters in regular waves. Ocean Engineering. 2015;104:370-86.
[16] Sheng W, Lewis A. Power takeoff optimization for maximizing energy conversion of wave-activated bodies. IEEE Journal of Oceanic Engineering. 2016;41:529-40.
[17] Zhang X, Yang J. Power capture performance of an oscillating-body WEC with nonlinear snap through PTO systems in irregular waves. Applied Ocean Research. 2015;52:261-73.
[18] Shi H, Zhao C, Liu Z, Cao F. Study on Hydraulic System Efficiency of Heaving-Buoy Wave Energy Converter. Journal of Ocean University of China. 2018;17:1044-52.
[19] Kurniawan A, Chaplin J, Greaves D, Hann M. Wave energy absorption by a floating air bag. Journal of Fluid Mechanics. 2017;812:294-320.
[20] Marquis L, Kramer M, Kringelum J, Chozas JF, Helstrup N. Introduction of Wavestar wave energy converters at the Danish offshore wind power plant Horns Rev 2. 4th international conference on ocean energy2012.
[21] Hansen RH, Kramer MM. Modelling and control of the wavestar prototype. The

9th European Wave and Tidal Energy Conference: EWTEC 2011: University of Southampton; 2011.
[22] Kim S-J, Koo W, Shin M-J. Numerical and experimental study on a hemispheric point-absorber-type wave energy converter with a hydraulic power take-off system. Renewable energy. 2019;135:1260-9.
[23] Sun L, Zang J, Stansby P, Moreno EC. Performance of the three-float wave energy converter M4 in regular and random waves. Progress in Renewable Energies Offshore: Proceedings of the 2nd International Conference on Renewable Energies Offshore (RENEW2016), Lisbon, Portugal, 24-26 October 2016: CRC Press; 2016. p. 269.
[24] Stansby P, Moreno EC, Stallard T, Maggi A. Three-float broad-band resonant line absorber with surge for wave energy conversion. Renewable Energy. 2015;78:132-40.
[25] Shi H, Li L, Zhao C. Optimization of wind-marine hybrid power system configuration based on genetic algorithm. Journal of Ocean University of China. 2017;16:709-15.
[26] Journée JM, Massie W. Offshore hydromechanics: TU Delft; 2000.
[27] Giorgi G, Ringwood JV. Analytical representation of nonlinear Froude-Krylov forces for 3-DoF point absorbing wave energy devices. Ocean Engineering. 2018;164:749-59.
[28] Barkhudarov MR. Lagrangian VOF Advection method for FLOW-3D. Flow Science Inc. 2004;1.
[29] ANSYS A. AQWA theory manual. ed Canonsburg, PA 15317, USA. 2013.
[30] Pastor J, Liu Y. Wave climate resource analysis based on a revised gamma spectrum for wave energy conversion technology. Sustainability. 2016;8:1321.
[31] Mei CC. Power extraction from water waves. Journal of Ship Research. 1976;20:63-6.
[32] António FdO. Modelling and control of oscillating-body wave energy converters with hydraulic power take-off and gas accumulator. Ocean engineering. 2007;34:2021-32.